5-2021

Constraining the Dark Matter in the Galaxy Lensing Quasar PG1115+080

Jackson Thomas Braley
Trinity University, jtbraley23@gmail.com

Constraining the Dark Matter in the Galaxy Lensing Quasar PG1115+080

by

Jackson T. Braley

An honors thesis submitted to the Department of Physics & Astronomy at

TRINITY UNIVERSITY

in partial fulfillment of the requirements for the

Bachelor of Science in Physics

May 2021

Accepted by .....
Prof. Kelvin Cheng

Accepted by .....
Prof. Nirav Mehta

Accepted by .....
Prof. David Pooley

Accepted by .....
Prof. Orrin Shindell

Accepted by .....
Prof. Jennifer Steele, Chair

Accepted by .....
Prof. Niescja Turner

Accepted by .....
Prof. Dennis Ugolini

Constraining the Dark Matter in the Galaxy Lensing Quasar PG1115+080

by

Jackson T. Braley

Submitted to the Department of Physics & Astronomy
on 2021-April-23, in partial fulfillment of the
requirements for the Bachelor of Science in Physics

Abstract

I present a microlensing analysis of 9 *Chandra* observations of the quadruply lensed quasar PG1115+080. Determinations of the microlensing effects in the lensing galaxy are carried out by finding the X-ray flux measurements of the individual quasar images via two-dimensional image fitting and spectral fitting. The results give a estimation of the local fraction of stellar matter making up the total integrated mass along the line of sight at an impact parameter of $\sim$ 6 kpc. A Bayesian analysis of microlensing maps and the measured X-ray flux of each image gives a most likely local stellar fraction of 4.64%, with the other 95.36% in a smooth, dark matter component.

Thesis Supervisor: Prof. D. Pooley

Acknowledgments

Thank you to the Physics and Astronomy department for supporting and guiding me through 4 years of education, research, and friendships. I would especially like to thank my advisor, Prof. David Pooley. I am fortunate to have found such a supporting, caring, and empathetic mentor, role model, and friend. In addition to being an excellent teacher of undergraduate physics courses, he has shown me the world of astrophysics and what it means to be the right partner to others.

I would also like to thank Prof. Orrin Shindell for introducing me to my next steps after graduation at The Land Institute in Kansas, where I will get into agricultural climate solutions. He has offered incredible support and insight during my times of struggle at Trinity, and guided me on my path to apply what I have learned in my physics education to fields of climate solutions.

None of this work would have been possible were it not for the love, care, and support offered to me by my parents, siblings, and closest friends throughout the ups and downs of my undergraduate career. I would be lost without you all.

Contents

Chapter 1

Introduction & Theory

Since Sir Arthur Eddington proved Einstein's general relativistic prediction that a massive body will gravitationally influence the path of light during the total solar eclipse on May 29, 1919, gravitational lenses have proved to be some of the most promising windows into the mysterious objects of the deep universe. Through the lensing of quasars, we are able to reveal insight into the structure of active galactic nuclei (AGN) and the dark matter to stellar matter content of lensing galaxies.

The primary focus of this project is to estimate the ratio of dark matter to stellar matter in the galaxy lensing the distant quasar PG1115+080 (hereafter, PG1115). The distribution of dark matter throughout individual galaxies and galaxy clusters has not been well-measured yet, but time-variable magnifications of lensed quasars as they move with respect to the lensing galaxy allow us to determine the most likely dark matter fractions in the lensing galaxy. This work builds on the previous work of (Pooley et al. 2006, 2009, 2012) and implements improved data analysis techniques. These techniques will be usefulf for the coming decade in which thousands of additional gravitationally lensed quasars will be found via the Vera C. Rubin Observatory, previously named the Large Synoptic Survey Telescope (LSST), (Chartas et al. 2020).

1.1 Quasars and Gravitational Lensing

Quasars, or quasi-stellar objects, are some of the furthest-observed objects in the universe, revealing insights into black hole formation in the early universe. Although synonymous with supermassive black holes (SMBH), they are distinguished by actively accreting matter. As one of the most energetic objects in the universe, the accretion disc radiates wavelengths across the electromagnetic spectrum. Their power outputs rival that of all other stars in their home galaxy, shining brighter than all the stars put together (Chartas et al. 2020; Moustakas et al. 2020; Pooley et al. 2020). While the detailed theory of quasar accretion discs are not fully understood, we have some understanding of the relative radii between emitting regions of different wavelengths. Several studies of lensed quasars analyze radio, optical, and even infrared wavelengths (Pooley et al. 2009; Weymann et al. 1980; Schechter & Wambsgnass 2003), but it is most useful to study these systems in the X-ray. The optical emitting region of the quasar is comparable in angular size to the Einstein radii of microlenses (see Equation 1.23 below), while the x-ray emitting region is much smaller (Chartas et al. 2020; Pooley et al. 2020, 2006, 2007, 2012; Schechter et al. 2014). Because X-rays come from regions much smaller than the Einstein radii of microlensing stars, they offer much clearer signals of microlensing than that of the optical. This allows us to probe closer to the event horizon of the black hole, tightening our grasp on the mechanics of accretion discs and AGN/galaxy evolution.

Although X-ray wavelengths permit us to probe closer to the event horizon of actively accreting SMBH, this is not the main purpose for this study of quasars in the X-ray. We focus on using the quasar as a background light source (Chartas et al. 2020; Pooley et al. 2020, 2012; Schechter & Wambsgnass 2003), whose variable brightnesses in X-ray data allows us to constrain the ratio of stellar matter to dark matter in the lensing galaxy. This is made possible by our understanding of gravitational lenses.

Much like how the base of a wine glass will create multiple lensed images of various magnifications of a candle behind it, massive galaxies can create multiple images of background quasars. While the wine glass analogy is effective at revealing the similarities between optical lensing observed on the surface of the Earth and gravitational lensing, the latter occurs at several different scales. Several studies of lensed quasars in recent decades reveal that simple, smooth mass models of lensing galaxies are sufficient at describing the overall surface density of matter in the lensing galaxy and predicting the locations of the multiple images of the background quasar (Pooley et al. 2006, 2007, 2009, 2012). They fail, though, in predicting the relative fluxes of the images. These flux-ratio anomalies are best explained by clumps of matter in the lensing galaxy that are doing further lensing. Previous studies have shown that those clumps are stars in the lensing galaxy, and the microlensing by those stars is the main contributor to brightnesses that vary on human time-scales (Chartas et al. 2020; Pooley et al. 2020; Moustakas et al. 2020; Pooley et al. 2007; Tie & Kochanek 2018).

In addition to macro- and microlensing, millilensing comes from the contribution of dark matter halos of masses $10^4 - 10^6\ M_\odot$(Pooley et al. 2009). The variability in millilensing effects, though, does not happen on human timescales like microlensing, and it also does not explain the differences in flux ratios when comparing X-ray and optical data.

1.2 Lensing Models

Past studies of gravitational lenses have lead to in-depth understanding of lens models. In order to examine properties of the lensing galaxy, we first define a potential function based on our model shape. From there, we create a deflection angle field, fit it into the lens equation, and make it dimensionless. The solutions to the lens equation give us the position of images, from which we find the magnification, convergence, and shear of each image (Meneghetti 2016; Kockanek 2004). Schechter et al., show that unlike optical data, the angular size of the X-ray emitting region is so small relative to the Einstein radii of stars that we can model the quasar as a point source (Schechter et al. 2014). Meneghetti's 2016 lecture of gravitational lensing and Kochanek's 2004 lecture on strong gravitational lensing give general reviews of these models (Meneghetti 2016; Kockanek 2004). The following sections are adapted from these lectures.

Any extended mass distribution is characterized by its effective lensing potential Ψ, which is obtained by projecting the three dimensional Newtonian potential Φ on the lens plane:

$$\hat{\Psi}(\vec{\theta}) = \frac{D_{LS}}{D_S D_L}\frac{2}{c^2}\int \Phi(D_L\vec{\theta}, z)dz \tag{1.1}$$

where D_{LS}, D_L, and D_S are defined in Figure 1-1. The dimensionless effective lensing potential $\Psi = \frac{D_L^2}{\zeta_0^2}\hat{\Psi}$ (ζ_0 is defined in Figure 1-1) is of more use in discovering the properties of the lens, such as the magnification, convergence, and shear. Once we have the dimensionless potential, we can find the scaled deflection angle by taking its gradient:

$$\vec{\nabla}_x\Psi(\vec{x}) = \vec{\alpha}(\vec{x}) \tag{1.2}$$

Futhermore, the Laplacian of Ψ gives us twice the convergence:

$$\Delta_x\Psi(\vec{x}) = 2\kappa(\vec{x}), \tag{1.3}$$

where the convergence is a dimensionless surface density

$$\kappa(\vec{x}) = \frac{\Sigma(\vec{x})}{\Sigma_{cr}}, \tag{1.4}$$

with the critical surface density $\Sigma_{cr} = \frac{c^2}{4\pi G}\frac{D_S}{D_L D_{LS}}$ characterizing the lens system as a function of the angular diameter distances of the lens and source.

For the lens equation $\vec{y} = \vec{x} - \vec{\alpha}(\vec{x})$ (derived in Section 2.2.1), the distortion of the images is described by its Jacobian matrix:

$$A = \frac{\delta\vec{y}}{\delta\vec{x}} = \left(\delta_{ij} - \frac{\delta\alpha_i(\vec{x})}{\delta x_j}\right) = \left(\delta_{ij} - \frac{\delta^2\Psi(\vec{x})}{\delta x_i \delta x_j}\right), \tag{1.5}$$

where x_i and x_j are the $i-$ and $j-$components of $\vec{x}$ on the lens plane. The magnification of images is given by the inverse of the determinant of the Jacobian:

$$\mu = \frac{1}{detA} \tag{1.6}$$

Meneghetti goes on to define

$$\Psi_{ij} = \frac{\delta^2\Psi(\vec{x})}{\delta x_i \delta x_j}, \tag{1.7}$$

so that we can split off an isotropic (equal physical property along each axis) part from the Jacobian:

$$\left(A - \frac{1}{2} trA \cdot I\right) = \delta_{ij} - \Psi_{ij} - \frac{1}{2}(1 - \Psi_{11} + 1 - \Psi_{22})\delta_{ij} \tag{1.8}$$

$$= -\Psi_{ij} + \frac{1}{2}(\Psi_{11} + \Psi_{22})\delta_{ij} \tag{1.9}$$

$$= \begin{pmatrix} -\frac{1}{2}(\Psi_{11} - \Psi_{22}) & -\Psi_{12} \\ -\Psi_{12} & \frac{1}{2}(\Psi_{11} - \Psi_{22}) \end{pmatrix} \tag{1.10}$$

The matrix in Equation 1.10 is called the shear matrix, quantifying the gradient of the gravitational force, or the gravitational tidal field. It describes distortions of background sources (Meneghetti 2016; Kockanek 2004). The shear components are that of a psuedo-vector defined on the lens plane $\vec{\gamma} = (\gamma_1, \gamma_2)$:

$$\gamma_1(\vec{x}) = \frac{1}{2}(\Psi_{11} - \Psi_{22}) \tag{1.11}$$

$$\gamma_2(\vec{x}) = \Psi_{12} = \Psi_{21}, \tag{1.12}$$

where the eigenvalues of the shear matrix are $\pm\sqrt{\gamma_1^2 + \gamma_2^2} = \pm\gamma$, resulting in a coordinate rotation by an angle φ:

$$\begin{pmatrix} \gamma_1 & \gamma_2 \\ \gamma_2 & -\gamma_1 \end{pmatrix} = \gamma \begin{pmatrix} \cos 2\varphi & \sin 2\varphi \\ \sin 2\varphi & \cos 2\varphi \end{pmatrix} \tag{1.13}$$

We now look at the remainder of the Jacobian:

$$\frac{1}{2} trA = \left[1 - \frac{1}{2}(\Psi_{11} + \Psi_{22})\right]\delta_{ij} \tag{1.14}$$

$$\left(1 - \frac{1}{2}\Delta\Psi\right)\delta_{ij} = (1 - \kappa)\delta_{ij} \tag{1.15}$$

Finally, the Jacobian reveals both the convergence and shear:

$$A = \begin{pmatrix} 1 - \kappa - \gamma_1 & -\gamma_2 \\ -\gamma_2 & 1 - \kappa + \gamma_1 \end{pmatrix} \tag{1.16}$$

$$= (1 - \kappa)\begin{pmatrix} 1 & 0 \\ 0 & 1 \end{pmatrix} - \gamma \begin{pmatrix} \cos 2\varphi & \sin 2\varphi \\ \sin 2\varphi & -\cos 2\varphi \end{pmatrix}. \tag{1.17}$$

The part of the distortion due to the convergence is constant in all directions, while the shear stretches the image only in one direction (Meneghetti 2016; Kockanek 2004). We can now descreibe the magnification as

$$\mu = \frac{1}{detA} = \frac{1}{(1 - \kappa)^2 - \gamma^2}. \tag{1.18}$$

Now that we have described the general properties of a lens (potential, deflection angle, magnification, convergence, shear), we can begin to look at specific lens models.

1.2.1 Point Mass Lensing

The basics of lensing are best understood through the treatment of a point mass lens, in which we begin with Fermat's Principle. In its simplest form, Fermat's Principle states that a given frequency of light will traverse the path between two points that takes the least time (Meneghetti 2016). Meneghetti goes through the point mass model of a lens, which can be seen in Figure 1-1, where the deflection angle is given by

$$\hat{\vec{\alpha}} = \frac{4GM}{c^2 b}\vec{e_r}, \tag{1.19}$$

where $\vec{e_r}$ is a unit vector in the radial direction. If θ, β, and $\hat{\vec{\alpha}}$ are very small, the three can be related to each other through the lens equation

$$\vec{\theta}D_S = \vec{\beta}D_S + \hat{\vec{\alpha}}D_{LS}. \tag{1.20}$$

This lens equation is further simplified through the introduction of the reduced deflection angle $\vec{\alpha}(\vec{\theta}) = \frac{D_{LS}}{D_S}\hat{\vec{\alpha}}(\vec{\theta})$, allowing Equation 1.20 to be rewritten as

$$\vec{\beta} = \vec{\theta} - \vec{\alpha}(\vec{\theta}), \tag{1.21}$$

where all the interesting physics comes from the fact that the deflection angle depends on $\vec{\theta}$ (Meneghetti 2016). Referring back to Equation 1.19, we set $b = D_L\theta$, resulting in

$$\beta = \theta - \frac{4GM}{c^2 D_L \theta}\frac{D_{LS}}{D_S}. \tag{1.22}$$

The Einstein radius of the point mass is given by $\theta_E = \sqrt{\frac{4GM}{c^2}\frac{D_{LS}}{D_L D_S}}$, allowing us to cast Equation 1.22 into

$$\beta = \theta - \frac{\theta_E^2}{\theta}. \tag{1.23}$$

By dividing through by θ_E, and setting $y = \frac{\beta}{\theta_E}$, and $x = \frac{\theta}{\theta_E}$, the lens equation reduces to its final form:

$$y = x - \frac{1}{x} \tag{1.24}$$

Multiply Equation 1.24 through by x, resulting in a quadratic equation where the image positions, $x_\pm$ are given by

$$x_\pm = \frac{1}{2}[y \pm \sqrt{y^2 - 4}] \tag{1.25}$$

If $y = 0$, the source is directly behind the lens, resulting in $x = 1 = \frac{\theta}{\theta_E}$, showing that the image takes on a ring shape with radius θ_E. If $\beta \to \infty$ (source far from lens) $\theta_- = x_-\theta_E = 0$, and $\theta_+ = x_+\theta_E \to \beta$, showing only an image at the source position and no lensed image, which is what we would expect for a source far from the lens.

The magnification μ of the images follows from the inverse of the determinant of the Jacobian $detA = \frac{y}{x}\frac{\partial y}{\partial x}$

$$detA = \left(1 - \frac{\alpha}{x}\right)\left(1 - \frac{\partial\alpha}{\partial x}\right) = \left(1 - \frac{1}{x^2}\right)\left(1 + \frac{1}{x^2}\right) = 1 - \left(\frac{1}{x}\right)^4 \tag{1.26}$$

$$\mu_\pm = \left[1 - (\frac{1}{x_\pm})^4\right]^{-1} = \frac{1}{2} \pm \frac{y^2 + 2}{2y\sqrt{y^2 + 4}}, \tag{1.27}$$

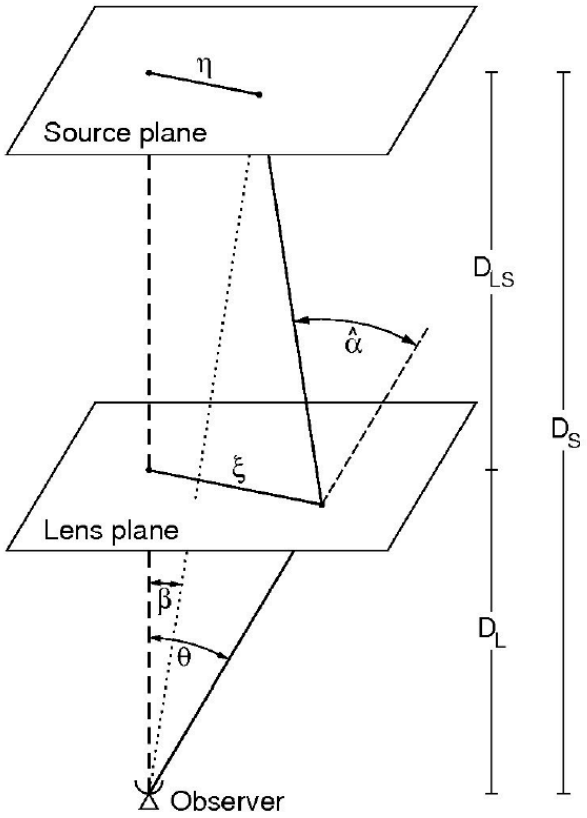

Figure 1-1: Typical gravitational lens, where D_L is the distance to the lens plane, D_S is the distance to the source plane, D_{LS} is the distance from the lens plane to the source plane, $\hat{\alpha}$ is the deflection angle, β is the source angular position which lies at a distance $\eta = \beta D_S$, θ is the angular position of the image, and $\zeta = \theta D_L$ is the impact parameter on the lens plane (from Meneghetti 2016).

where we notice $\lim_{y\to\infty}\mu_- = 0$ and $\lim_{y\to\infty}\mu_+ = 1$, although the lens equation has two solutions. For large angular separations between the source and the lens, one of the solutions to the lens equation disappears because it is demagnified, while the other has the same flux and position as the source, resulting in no lensing.

1.2.2 Singular Isothermal Sphere

While it is useful to understand lensing by a point mass, the lensing bodies of quasars are galaxies with extended masses. One of the most widely used extended, axially symmetric models is the Singular Isothermal Sphere (SIS hereafter) (Meneghetti 2016; Kockanek 2004). This model introduces a density profile that is derived based on the assumption that the matter content of the lens behaves as an ideal gas in thermal and hydrostatic equilibrium confined by a spherically symmetric gravitational potential (Meneghetti 2016). The three dimensional density profile of the lens is given by

$$\rho(r) = \frac{\sigma_v^2}{2\pi G r^2}, \tag{1.28}$$

where σ_v is the velocity dispersion of the gas particles (I use the term "gas" as it is consistent with the model, but let it be known that the matter content of the lens is not truly an ideal gas, but rather some combination of clumpy matter in the form of stars and smooth dark matter), and r is the distance to the sphere center. This model utilizes the thin screen approximation, seen in Figure 1-1, so we can turn any three dimensional mass density into a surface density by taking the integral:

$$\Sigma(\vec{\zeta}) = \int \rho(\vec{\zeta}, z)\, dz \tag{1.29}$$

By projecting the three dimensional density, Equation 1.28, along the line of sight, we arrive a two dimensional surface density:

$$\Sigma(\zeta) = 2\frac{\sigma_v^2}{2\pi G}\int_0^\infty \frac{dz}{\zeta^2 + z^2} = \frac{\sigma_v^2}{\pi G \zeta}\Big[\arctan\frac{z}{\zeta}\Big]_0^\infty \tag{1.30}$$

$$\Sigma(\zeta) = \frac{\sigma_v^2}{2G\zeta} \tag{1.31}$$

Notice that when $\zeta = 0$, the density profile has a singularity, where it is seemingly infinite in density. This singularity is purely mathematical, having no physical meaning. Nonetheless, this model is efficient in describing the matter distribution in galaxies (Meneghetti 2016). Meneghetti goes on to choose a length scale on the lens plane $\zeta_0 = 4\pi\left(\frac{\sigma_v}{c}\right)^2 \frac{D_L D_{LS}}{D_S}$ in order to cast the surface density as a function of x:

$$\Sigma(x) = \frac{\sigma_v^2}{2G\zeta}\frac{\zeta_0}{\zeta_0} = \frac{1}{2x}\frac{c^2}{4\pi G}\frac{D_S}{D_L D_{LS}} = \frac{1}{2x}\Sigma_{cr} \tag{1.32}$$

The convergence of the singular isothermal sphere follows from Equation 1.4 as

$$\kappa(x) = \frac{1}{2x}, \tag{1.33}$$

and the lensing potential follows from the dimensionless version of Equation 1.1 as

$$\Psi(x) = |x|. \tag{1.34}$$

From Equation 1.2, the deflection angle is

$$\alpha(x) = \frac{x}{|x|} \tag{1.35}$$

resulting in the lens equation

$$y = x - \frac{x}{|x|}. \tag{1.36}$$

The shear follows from the derivatives of the potential (Equation 1.7):

$$\frac{\delta\Psi}{\delta x_i x_j} = \frac{\delta_{ij}x^2 - x_i x_j}{x^3} \tag{1.37}$$

Leading to

$$\Psi_{11} = \frac{x_2^2}{x^3} \tag{1.38}$$

$$\Psi_{12} = -\frac{x_1 x_2}{x^3} \tag{1.39}$$

$$\Psi_{22} = \frac{x_1^2}{x^3} \tag{1.40}$$

The shear components (Equations 1.11 and 1.12) are

$$\gamma_1 = \frac{1}{2}\frac{x_2^2 - x_1^2}{x^3} = \frac{1}{2}\frac{\sin^2\varphi - \cos^2\varphi}{x} = -\frac{1}{2}\frac{\cos 2\varphi}{x} \tag{1.41}$$

$$\gamma_2 = -\frac{\cos\varphi \sin\varphi}{x} = -\frac{1}{2}\frac{\sin 2\varphi}{x} \tag{1.42}$$

And thus the total shear

$$\gamma(x) = (\gamma_1^2 + \gamma_2^2)^{1/2} = \frac{1}{2x} = \kappa(x) \tag{1.43}$$

Finally, the magnification as a function of image position follows from Equation 1.36:

$$\mu = \frac{|x|}{|x| - 1} \tag{1.44}$$

1.2.3 Occurrence of Images

The deflection of light rays due to the gravitational influence of the lensing galaxy causes a delay in the amount of time it takes for radiation to reach the observer (Meneghetti 2016; Kockanek 2004). One part of this time delay is due to the different path lengths between the deflected light ray and an unperturbed one. This geometrical difference is proportional to the squared angular separation between the source position and the image position. The other part of the time delay is due to the slowing of photons travelling through a gravitational field. Thus, it is related to the gravitational potential. A lens at redshift z_L gives a total time delay as a function of position $\vec{x}$ on the lens plane

$$t(\vec{x}) = \frac{(1+z_L)}{c}\frac{D_S\zeta_0^2}{D_L D_{LS}}\left[\frac{1}{2}(\vec{x} - \vec{y}) - \Psi(\vec{x})\right] \tag{1.45}$$

This equation shows that images follow Fermat's Principle: $\nabla t(\vec{x}) = 0$. Thus, images are located at the stationary points of the time delay surface (Equation 1.45). The matrix of all the second-order partial derivatives of the surface,

or the Hessian matrix, is given by

$$T = \frac{\delta^2 t(\vec{x})}{\delta x_i \delta x_j} \tag{1.46}$$

This matrix is proportional to $\delta_{ij} - \Psi_{ij}$, thus leading us to distinguish a variety of image types.

Meneghetti defines three types of images that arise on the time delay surface. Type I images are at the minima of the time delay surface, where the eigenvalues of the Hessian matrix are positive. These images have positive magnification. Type II images are at the saddle points of the time delay surface, where the eigenvalues of the Hessian matrix are of opposite signs. These images have negative magnifications, which we interpret as the image being flipped relative to the source. Lastly, type III images are at the maxima of the time delay surface, where both eigenvalues of the Hessian matrix are negative. These images are strongly demagnified and are rarely observed.

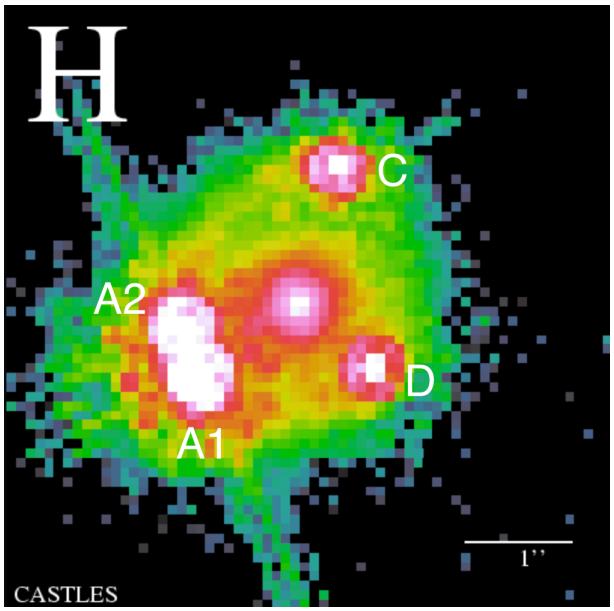

Figure 1-2: Photo of PG1115 in the optical. Image A1 is the HM image, A2 is the HS, C is the LM, and D is the LS image. This photo is from the CfA-Arizona Space Telescope LEns Survey of gravitaional lenses (CASTLES) (from C.S. Kochanek, E.E. Falco, C. Impey, J. Lehar, B. McLeod, H.-W. Rix).

1.3 Past Work on PG1115+080

This project dives into one system, quasar PG 1115+080 (hereafter, PG1115). Shortly after the discovery of the first gravitational lens (Chang & Refsdal 1979), PG1115 was discovered as the first quadruply lensed (quad) system (Weymann et al. 1980). The initial report discussed the system as a triple image system because two of the images are nearly identical in position. The four images of a quad system are either minima or saddle points of the light travel time surface (Meneghetti 2016; Kockanek 2004). The two minima images have different magnifications, where the higher is denoted HM and the lower LM. Similarly, the two saddle point images have different magnifications, where the higher is denoted HS, and the lower LS. Weymann et al. incorrectly assumed PG1115 was a triple because the higher magnified minima (HM) and higher magnified saddle point (HS) are so close to each other ($\sim$ 0.5" apart).

The source of PG1115 is located at redshift z=1.72, while the lens is located at redshift z=0.31 (Weymann et al. 1980). Pooley et al. in 2006 used one main singular isothermal sphere to model the lens, with the addition of a second singular isothermal sphere to represent a group of galaxies to the southwest of the lensing galaxy (Pooley et al. 2006) in order to confirm the source of variable magnifications as microlensing in X-rays rather than optical. The discussion of the source of time varibale magnifications can be found in Section 2.1. This model gives a predicted A2/A1 ratio of 0.96 $\pm$ 0.05 (Pooley et al. 2006). In 2007, Pooley et al. used one singular isothermal sphere with an external shear, giving a predicted A2/A1 ratio of 0.92. The observed ratio in the optical has fallen in the range of 0.65-0.85 since its first measurements, but Pooley et al. favor the model with two isothermal spheres because it has a lower chi-sqaured and takes into account the environment of the lens galaxy (Pooley et al. 2009). Schechter et al. use similar models to that of Pooley et al. in 2007, modeling several galaxies as singular isothermal ellipsoids with external shears (Schechter et al. 2014).

In 2009, the most likely dark matter to stellar matter ratio in the lensing galaxy of PG1115 was 90% dark

matter to 10% stellar matter (Pooley et al. 2009). In 2012, Pooley et al. combined their analysis of 13 quadruple lens systems to find a most likely ratio of 93.2% smooth dark matter to 6.8% clumpy stellar matter at an impact parameter of 6.6 kpc (Pooley et al. 2012). While they report a combined analysis of 13 different systems, their individual analysis of PG1115 resulted in a most likely ratio of 95.4% dark matter to 4.6% stellar matter.

These probabilities would not be made possible without the time-variable microlensing affects of image A2, the highly demagnified saddle point. The first two X-ray observations of PG1115 in 2000 resulted in A2/A1 ratios of 0.16 ± 0.03 and 0.29 ± 0.08 (Pooley et al. 2009). These ratios are due to the A2 image being dramatically demagnified at the time of observations. The stark differences in the A2/A1 X-ray ratio over time in comparison to the nearly constant optical ratio show that microlensing effects are greatest in the X-ray emitting regions of the quasar rather than the optical.

1.4 Chandra Specifications, Observations, and Data Reduction

All observations of PG1115 were taken by the *Chandra* X-ray Observatory, NASA's flagship mission for X-ray astronomy. Launched on July 23, 1999, *Chandra* orbits the Earth up to an altitude of $139,000$ km because X-rays are absorbed by the Earth's atmosphere, making a ground-based telescope inefficient for detecting X-rays. Of the various scientific instruments on board *Chandra* , all observations were taken with the telescope aimpoint on the Advanced CCD Imaging Spectrometer (ACIS) S3 chip. This back-illuminated 1024x1024 pixel chip has an imaging resolution of 0.5" over the energy range 0.2-10 keV, and a sensitivity of 4×10^{-15} erg cm^{-2} s^{-1}in 10^5 seconds.

All data reduction were performed using the *Chandra* Interactive Analysis of Observations (CIAO) software, version 4.13. Prof. David Pooley performed all data reduction and reprocessing, creating event files for each observation.

Chapter 2

Methods and Results

2.1 Flux Determinations

The individual fractions of the total flux of each observation were extracted via two-dimensional image fitting. SHERPA is Chandra's Interactive Analysis of Observation (CIAO's) modeling and fitting application, which allows users to construct complex models and fit those models to data. Sub-pixel resolution images of the event files are loaded into SHERPA . In all of our image fitting, we use Cash statistics ('cash' in SHERPA) (Cash 1979), and the

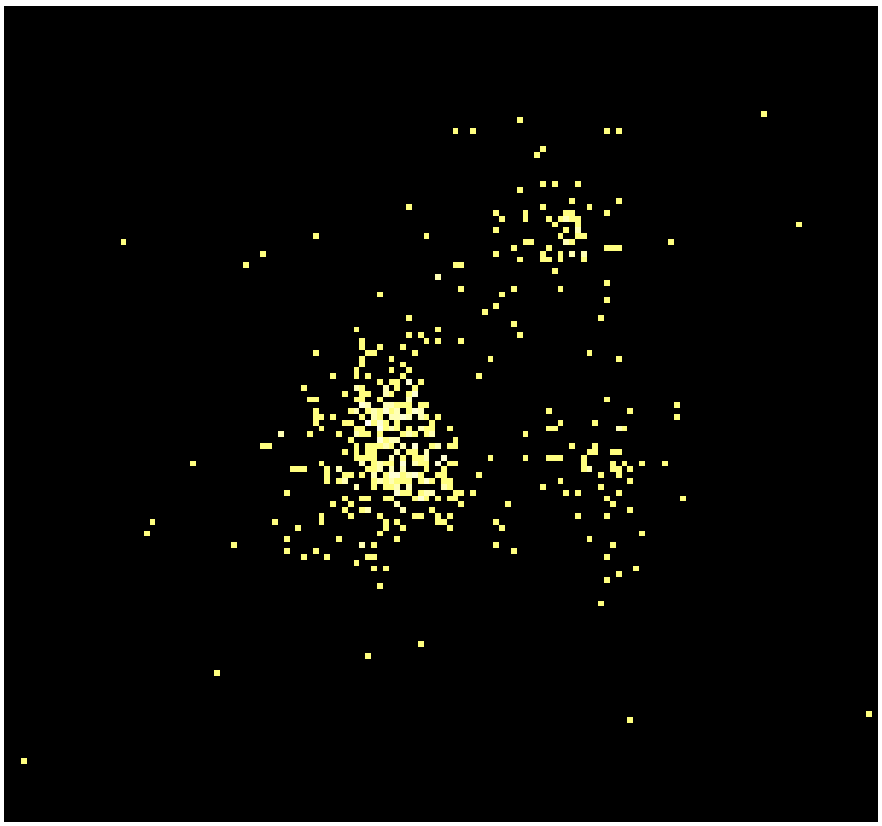

Figure 2-1: Sub-image of reprocessed data for obsid 10730. The image is binned to 0.1 pixel size, and energy is filtered to the range 400-8000 keV.

Nelder & Mead optimization method ('simplex' in SHERPA) (Nedler & Mead 1965). The Cash statistic is a maximum

likelihood function where counts are sampled from the Poisson distribution. It is determined by (1) taking the logarithm of the likelihood function (product of individual Poisson probabilities in each bin), (2) changing its sign, (3) dropping the factorial term, and (4) multiplying by two:

$$C = 2\Sigma_i[M_i - D_i log M_i] \tag{2.1}$$

where $M_i = S_i + B_i$ is the sum of source and background model amplitudes, and D_i is the number of observed counts in bin *i*. The change in Cash statistic from one model fit to the next is distributed approximately as $\Delta\chi^2$. The background does not need to be subtracted from the data while using this statistic, allowing for a simultaneous modeling of the background with the source. The simplex method directly finds the minima relative to an initial starting position, as opposed to the Monte Carlo method which starts with a random sampling of points and updates with each iteration to find local minima of the fit statistic. The relative positions of each image were fixed to the separations given in the CASTLES online database (see Figure 1-2), which were determined using observations from the *Hubble Space Telescope*. The values given by CASTLES are converted into image pixels to feed into SHERPA . The positions of images A1, A2, and B are given relative to image C. The initial position of image C is determined using the best guess of the image coordinates in the imaging software, SAOImage DS9.

Originally, I fit each image with a simple two-dimensional normalised gaussian function ('normgauss2d' in SHERPA). This model has several parameters, some of which I froze and others I thawed and defined in relation to image C. The Full-Width Half Maximum (FWHM) of the gaussian for each image was thawed and set equal to the FWHM of image C. The x- and y-positions of images A1, A2, and B are set using their positions relative to image C, as discussed above. The initial location of image C was manually defined in image coordinates. The minimum amplitude of each gaussian, or the integral of the model over a range $-\infty$ to ∞ for both axes, was changed from its default setting of -3.40282×10^{38} to 0 for each image. The ellipticity of the gaussian and angle of the major axis θ were set to their default settings of 0 and frozen. I fit each observation with this model, and switched back and forth between using the Cash statistic and Monte Carlo ('moncar' in SHERPA) in order to ensure that I've found the global minumum for each image.

2.1.1 Accounting for Point Spread Function Effects

Although 2D gaussians were a good starting point, the Chandra point-spread function is not a gaussian in shape and is much more sharply peaked. I accounted for the effects of the point spread function (PSF) and added a constant two-dimensional background model ('const2d' in SHERPA). Due to quantum mechanics, any imaging device will have a response to a point source that results in a blurring effect across the detector.

The *Chandra* PSF is energy dependent and varies in size and shape across the field of view. Near the optical axis, the PSF can be less than one arcsecond, while it is much larger at the extreme edges of the detector. The Chandra Ray Tracer (hereafter, ChaRT) (Carter et al. 2003) produces the best available PSF for a source at any off-axis angle and for any specified energy or spectrum. ChaRT traces rays through *Chandra* X-ray Optics, and then projects them onto the detector via MARX. The result is an event file from which an image of the source can be created. The process is outlined by (1) preparing the inputs to run ChaRT, (2) running ChaRT, (3) retrieving the ray file, (4) creating an event file, and (5) creating an image of the PSF.

The ChaRT inputs include the off-axis angles θ (arcminutes) and φ (degrees), a spectrum file, the detector

pointing information (right ascension, declination, roll, and exposure), and how many iterations the user desires. Multiple iterations can be averaged to create the best possible image of the PSF.

I created a PSF for each observation. The source coordinates are obtained using the 'dmcoords' command in CIAO. For each observation, I extracted a spectrum using 'specextract' in SHERPA . This creates a source and background spectra from source and background regions in the reprocessed event file (see Figure 2-2). This results in separate files for the auxiliary response (ARF, contains the effective area of the detector and quantum efficiency as a function of energy over time), and the redistribution matrix (RMF, spreading of observed counts across detector via matrix multiplication) for both the source and background. Then, I fit the spectrum by loading it into a SHERPA session, which automatically uploads the ARF and RMF files for the source and background. Using the 'cstat' statistic and 'simplex' model with an energy range of 0.3-8.0 keV, I fit the spectrum using a simple power law. The resulting spectrum file can be seen in Figure 2-3. This spectrum does not take into account the absorption of the milky way, but works well for creating the PSF. I take into account the Milky Way absorption in the next section. Lastly, I find the nominal pointing information for each observation, set the exposure to 200 ksec, and set the number of iterations to 50.

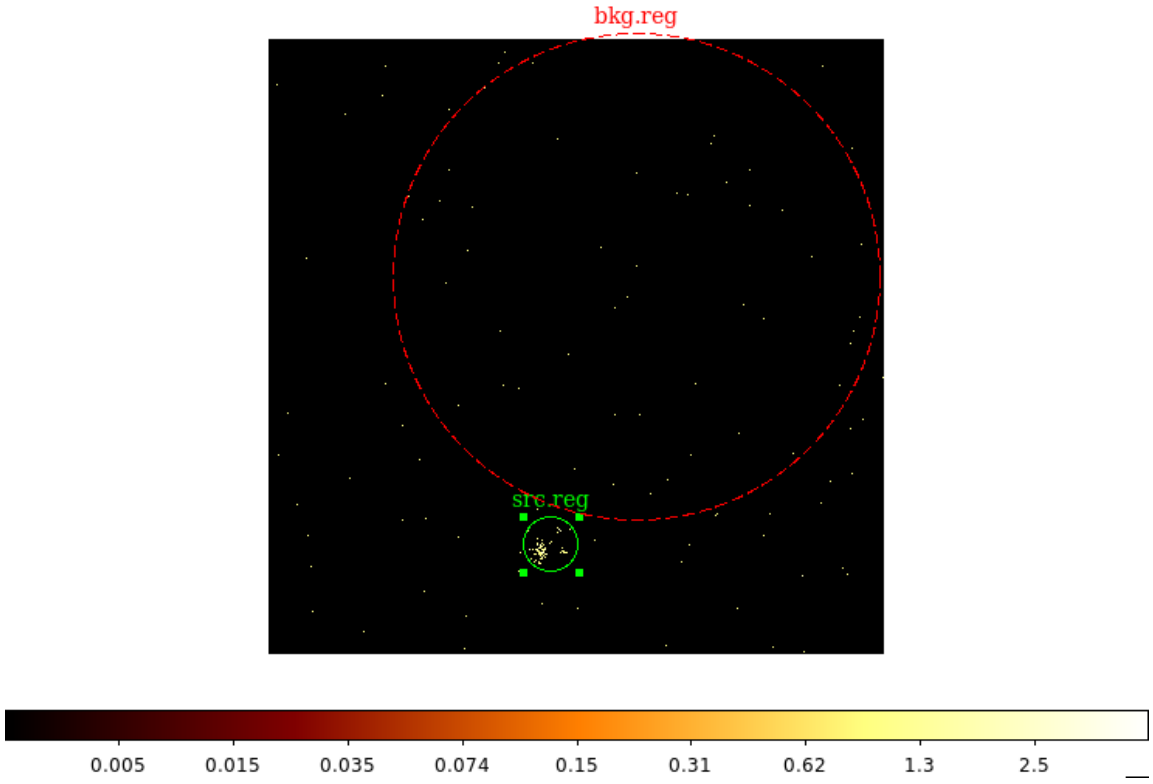

Figure 2-2: Source (src.reg) and Background (bkg.reg) regions for obsid 10730. These were created in the reprocessed event file with bins of size 0.1, log scale, and energy filtered to 0.4-8.0 keV.

The results of running ChaRT are a tar file with one fits file for each iteration in it. I create an event file from each fits file using MARX software. This software requires the nominal pointing right ascension, declination, roll, and the source right ascension and declination. I merge all of the event files to create one image file of the PSF for a given obsid. Figure 2-4 shows the resulting PSF for obsid 10730.

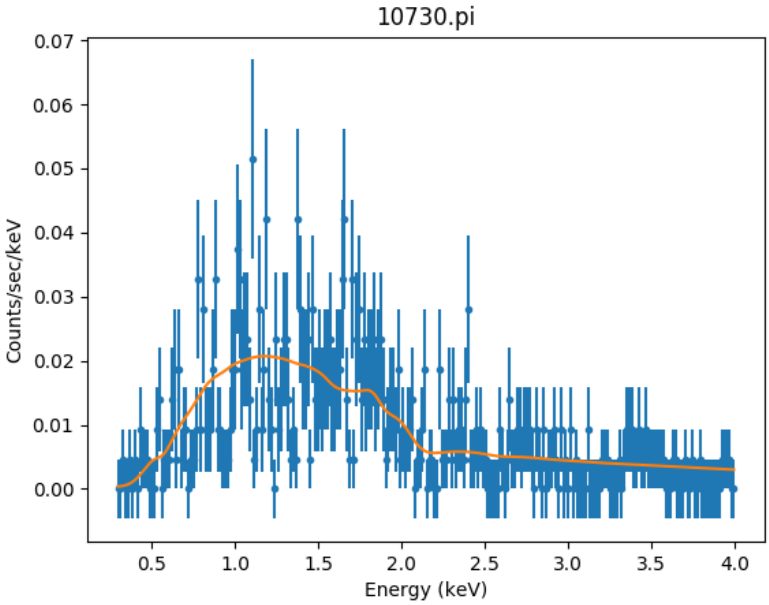

Figure 2-3: Extracted spectrum file for obsid 10730 to input to ChaRT

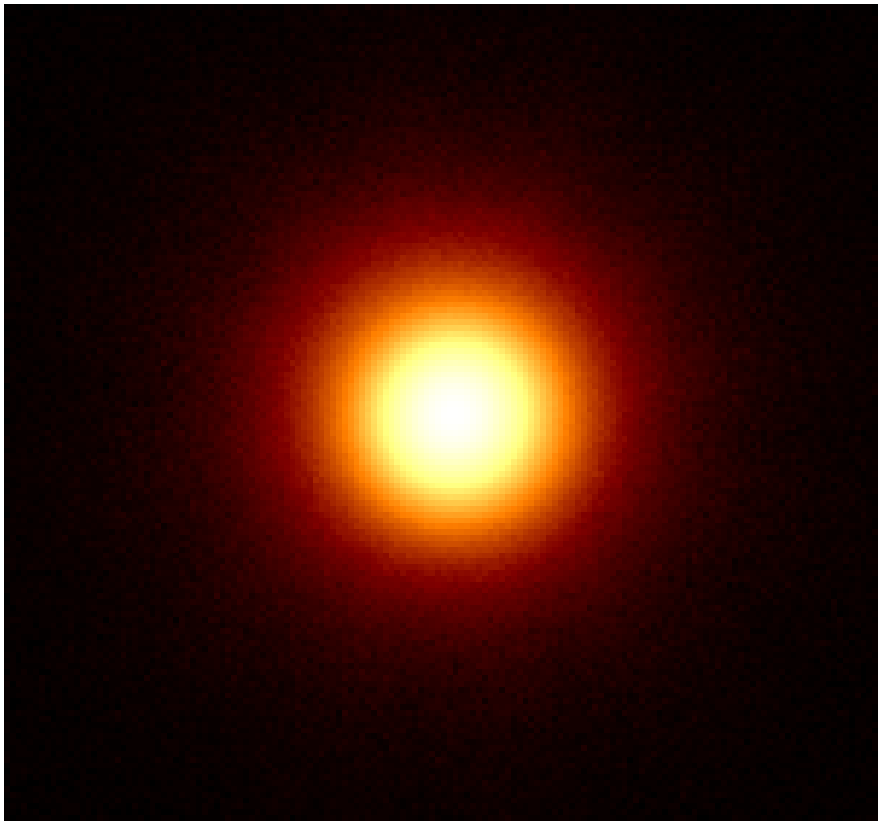

Figure 2-4: Point spread function of PG1115 for obsid 10730. This image has been trimmed to be the same region in the sky as Figure 2-1

2.1.2 Updated Model with PSF

Before fitting the images with the PSF, I load both the PSF and sub-image (Figure 2-1) side-by-side in order to check their positions in image coordinates. In creating the PSF for all observations, some were outside the region in the sky that contained the images. This is because of error while inputting the source and pointing information into ChaRT. After retracing the rays in ChaRT with the correct information, I ensured each PSF was in the correct region of the sky to produce four images. Then, I fit each image with the PSF in a SHERPA session. In SHERPA , there is an option to load a PSF and set it in the model ('load_psf' and 'set_psf'). I used the 'cstat' statistic, which is the implementation of the 'cash' statistic described above within the XSPEC module in SHERPA . Just like 'cash', the background should not be subtracted from the data for this statistic. I then set the method to 'neldermead', which is equivalent to the 'simplex' model described above. Within the 'neldermead' optimization method, I set 'iquad' to 0, which indicates that a fit to a quadratic surface was not done. Additionally, I set 'finalsimplex' to 0, which specifies whether the simplex has converged. The positions of images A1, A2, and B were once again given relative to image C from CASTLES. The amplitude of the constant two-dimensional background model was set to 0, and the FWHM of each image was set to 1. Both of these parameters were frozen for the fit.

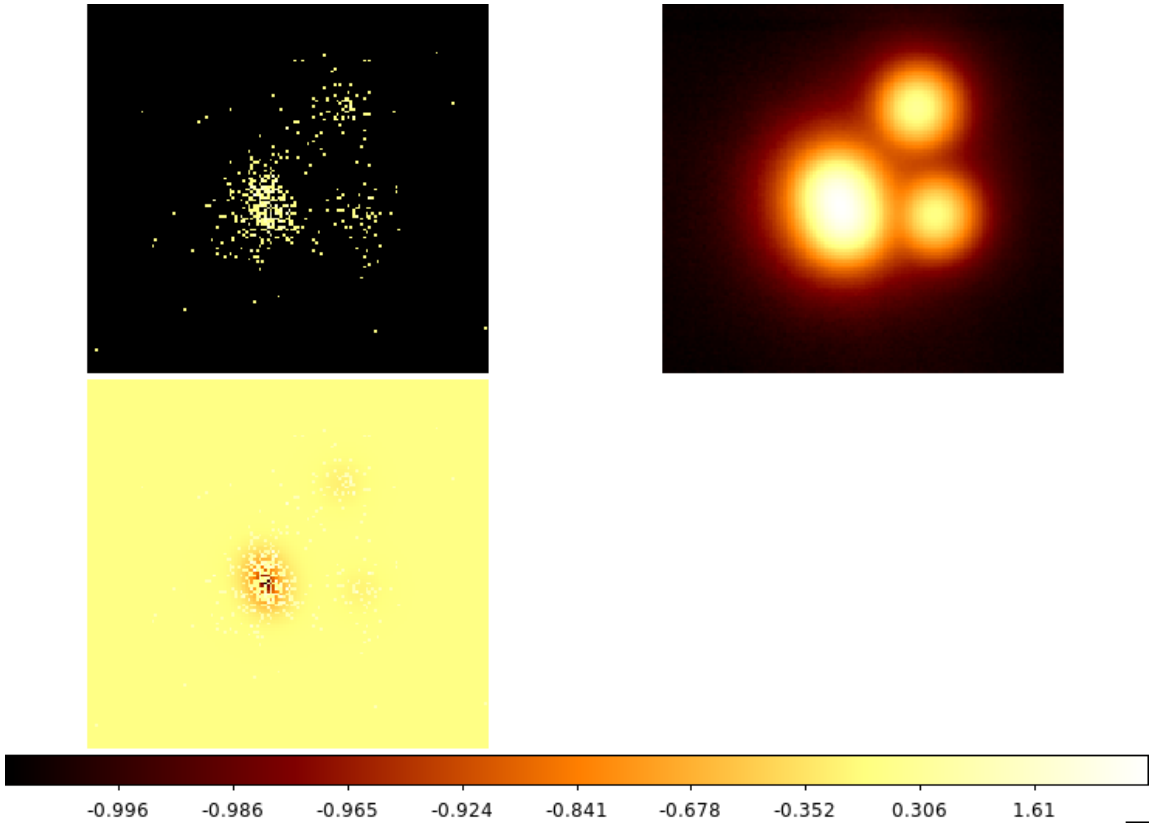

Figure 2-5: *Top left:* Reprocessed data projected onto the detector. *Top right:* The two-dimensional gaussian fit of the data with the PSF accounted for. *Bottom left:* Residuals.

I fit this model several times until the change in fit statistic was 0. The resulting image fit of obsid 10730 can be seen in Figure 2-5. The upper left panel is the reprocessed, binned data with an energy filter of 0.4-8.0 keV seen in Figure 2-1. The upper right image is the resulting two-dimensional gaussian fit with the PSF accounted for. The bottom left panel is the residuals. The residuals for images B and C are insignificant, while there is some structure

around images A1 and A2 which likely indicates an imperfect PSF shape and will be studied in the future. The flux ratios for each observation are given in Table A.3.

2.2 Spectral Analysis

I determine the flux of each image by multiplying a spectral fit of all images combined by their individual flux ratios. For each observation, I extracted the spectrum of a large region enclosing all four images, as well as a larger region of the background.

The source and background regions of obsid 10730 are seen in Figure 2-2. The circular source region has a radius of 2.283", while the larger background region has a radius of 19.93". The radii of source and background regions for the other observations are given in Table A.2.

The source and background events were modelled simultaneously using an absorbed, independent power law. The absorption column density was set at the Galactic value in the direction of the lens, which is $3.18{\times}10^{20}\ \frac{atoms}{cm^2}$ for PG1115. We follow a similar method to the spectral extraction used in the PSF in section 2.2.1. In a SHERPA session, I loaded the spectrum file, which automatically uploads the RMF and ARF files of the source and background regions. Using the 'cstat' statistic and 'simplex' optimization method, I fit the spectrum in an energy range of 0.4–8.0 keV.

Fitting these spectra with a simple absorbed power law are only meant to produce a gross X-ray spectral shape for flux estimation. It does not take into account extragalactic absorption or spectral emission lines. Some systems require the addition of an emission line model, such as my work with Q2237+030 over the summer of 2019, which produced a relativistic iron line. While this simple model does not allow for such features, the reduced fit statistics indicate more the adequate agreement between the simple models and the X-ray data.

The uncertainties in the fits were calculated using the SHERPA tool 'sample_energy_flux.' This tool uses 1000 samples of the power-law index and amplitude from the normal distribution in order to calculate 1000 values for the flux. The uncertainties are reported with the total fluxes of each observation in Table A.3.

An updated spectral fit is seen in Figure 2-6. The lower range of 0–0.4 keV is excluded because the detector rapidly loses sensitivity below 0.4 keV.

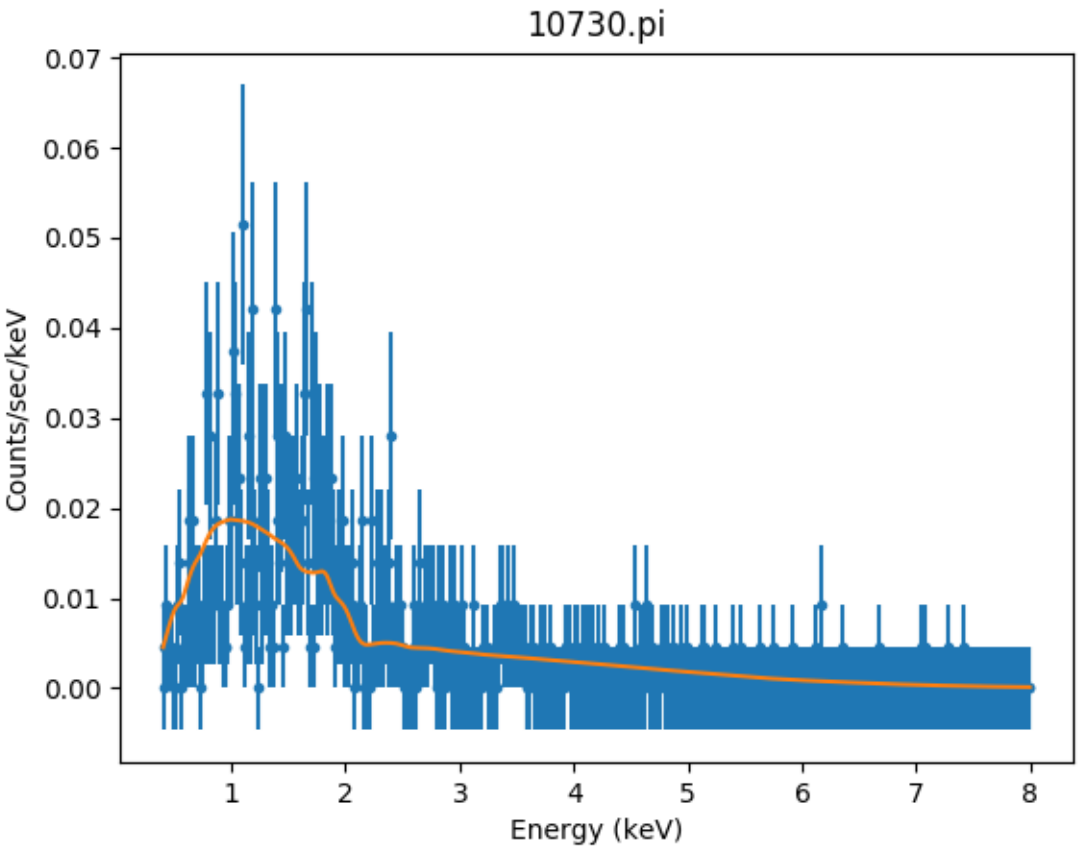

Figure 2-6: Updated spectral fit for obsid 10730 over the energy range 0.4-8.0 keV

Chapter 3

Dark Matter Determinations

3.1 Microlensing Maps

As mentioned in Section 1.1, microlensing leads to time-variable brightnesses of individual images. These variations are due to relative movement of the background quasar with respect to individual stars in the lensing galaxies.

Large scale models give us the local convergence κ and shear γ for each image, which produces the macrolesning magnification of each image. These values are given in Table A.1. These models give the total convergence at the location of each image without regards to the form of the matter. We assume different values of stellar to dark matter in the galaxy to produce several microlensing maps. Previous studies of these observations utilized microlensing maps created by the ray-tracing code of Wambsganss (1990). This project follows the same process for determining dark matter distributions, but utilizes updated microlensing maps. The new maps were created by Jordan Koeller for his undergraduate thesis in the Physics and Astronomy department.

I used 12 microlensing maps of each of the four images, resulting in a total of 48 maps. The 12 different maps are associated with different fractions of stellar matter to dark matter. These stellar fractions (S_j) follow a logarithmic sequence: 1.47%, 2.15%, 3.16%, 4.64%, 6.81%, 10%, 14.68%, 21.5%, 31.62%, 46.4%, 68.13%, and 100%. These magnification maps are constructed on the source plane with their centers referenced to the location of one of the quasar images. They produce the effects of microlensing magnifications for a source located anywhere within the map. The macrolensing effects (due to smooth lensing potential) has been subtracted off. Each map is 2000 x 2000 pixels.

Within the maps exist caustic lines, which are the lines of sharp change in magnification. Every caustic is a closed curve, showing higher magnifications inside and lower outside. The lines are of 0 width and correspond to the magnification diverging to infinity. A source position crossing a caustic corresponds to the creation or termination of two images. The points of caustic curves are cusps, while the curved segments are folds.

Figures 3-1, 3-2, 3-3, and 3-4 show the magnification maps for the higher minima image, higher saddle image, lower minima image, and lower saddle image respectively. The top map in each of these figures correspond to a stellar fraction $S_j = 10\%$ while the bottom maps correspond to a stellar fraction $S_j = 100\%$. There exist maps for each of the stellar fractions mentioned above, but I show these two fractions to highlight the differences in microlensing magnifications across different stellar fractions.

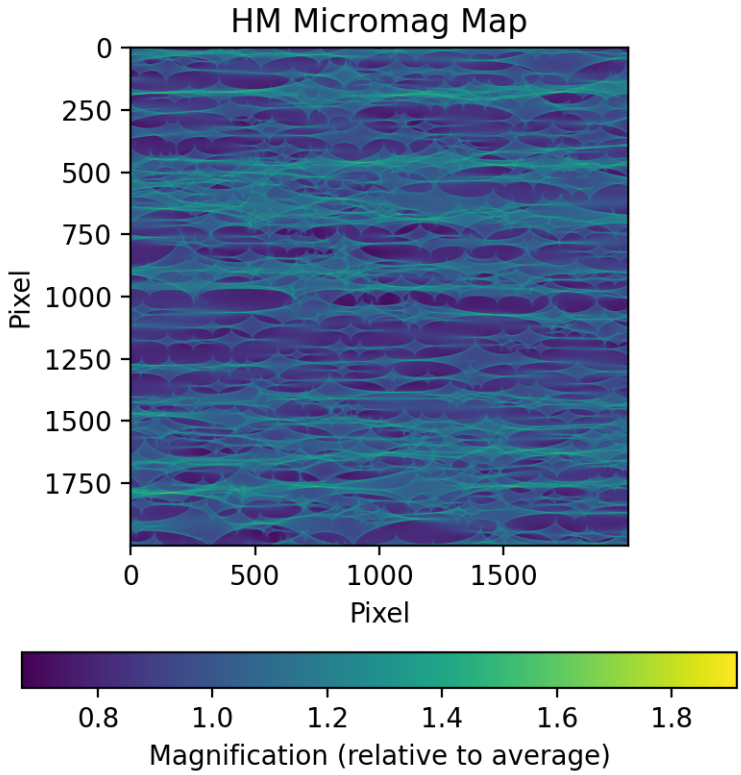

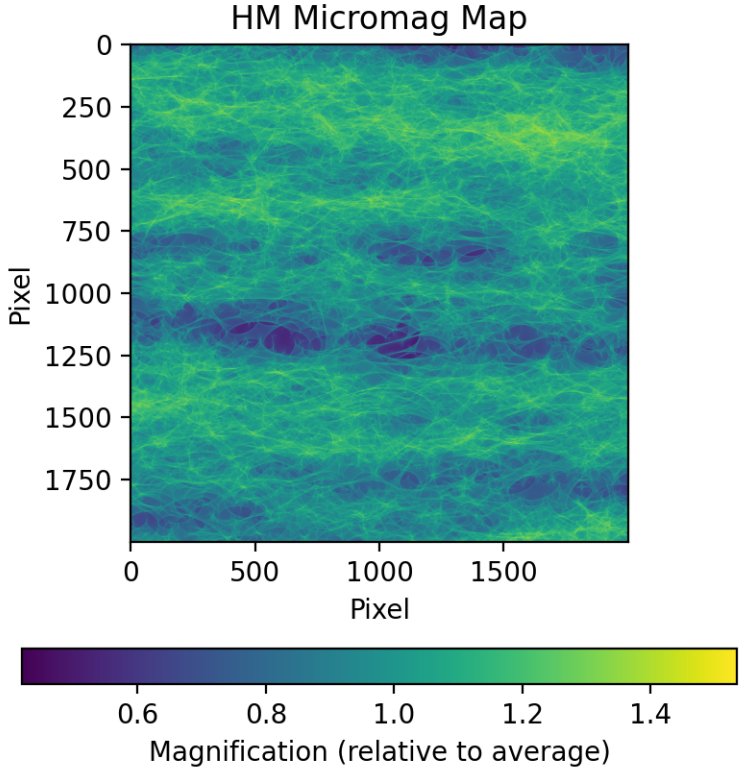

Figure 3-1: *Top:* Magnification map for the higher minima image for $S_j = 10\%$ *Bottom:* Magnification map for the higher minima image for $S_j = 100\%$

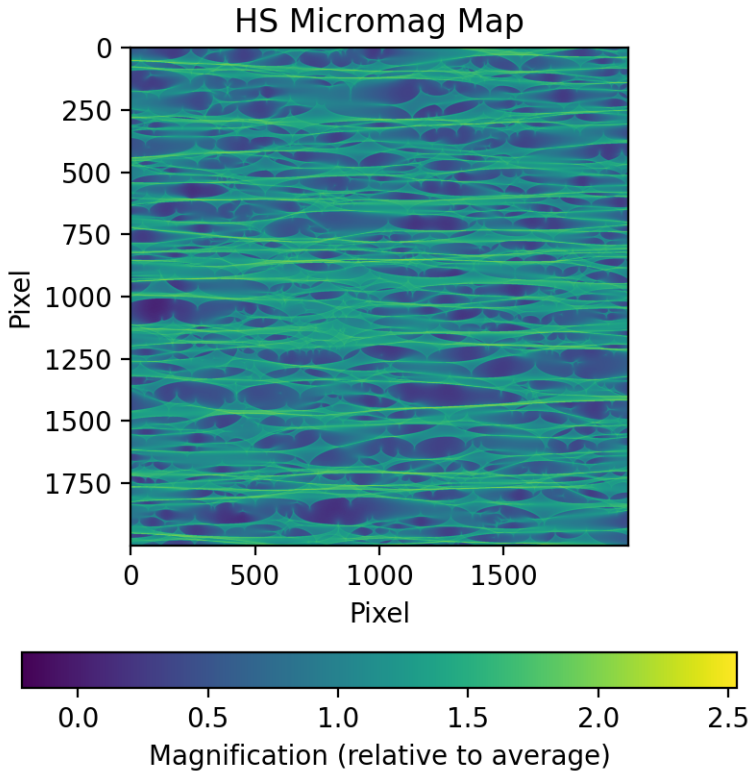

Figure 3-2: *Top:* Magnification map for the higher saddle image for $S_j = 10\%$ *Bottom:* Magnification map for the higher saddle image for $S_j = 100\%$

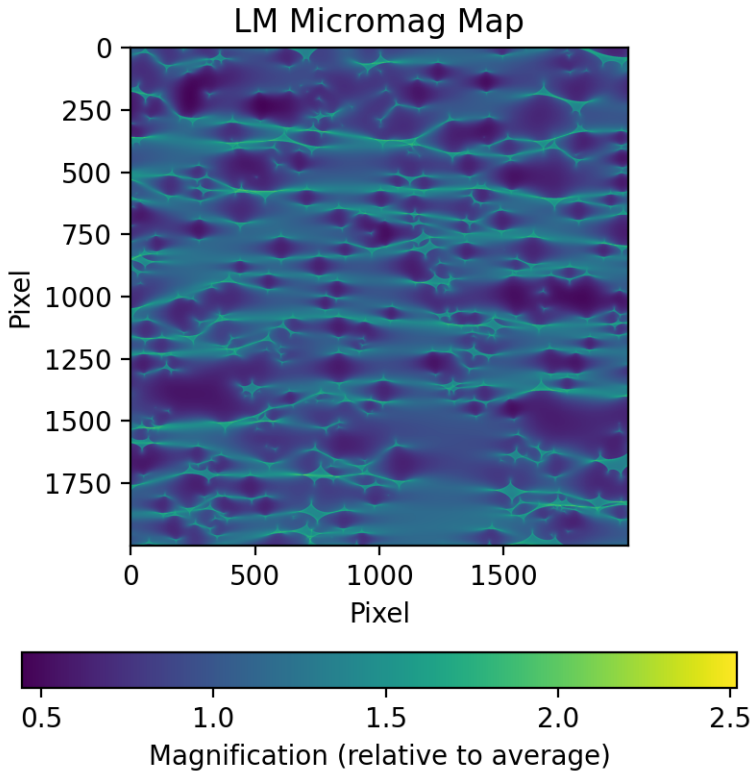

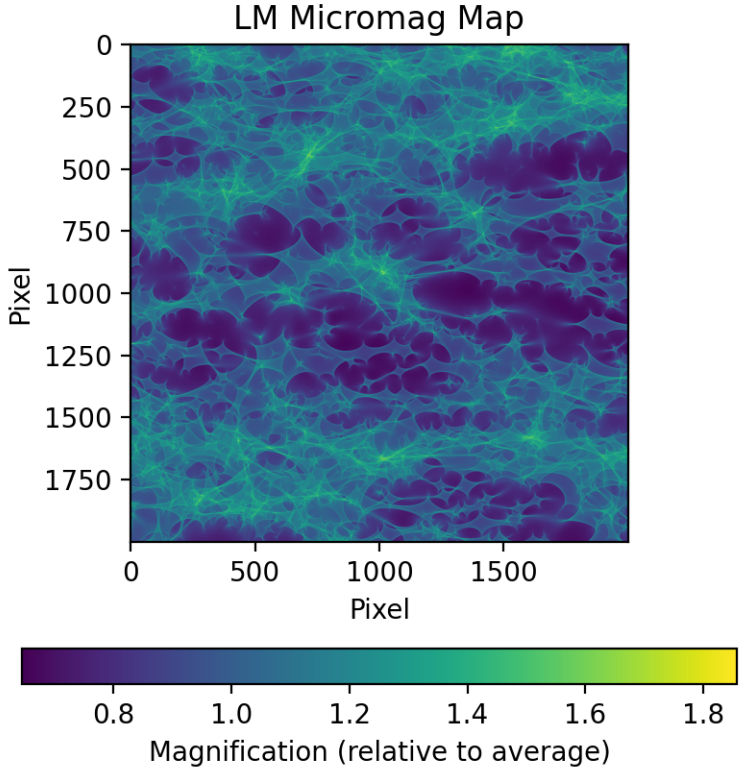

Figure 3-3: *Top:* Magnification map for lower minima image for $S_j = 10\%$ *Bottom:* Magnification map for lower minima image for $S_j = 100\%$

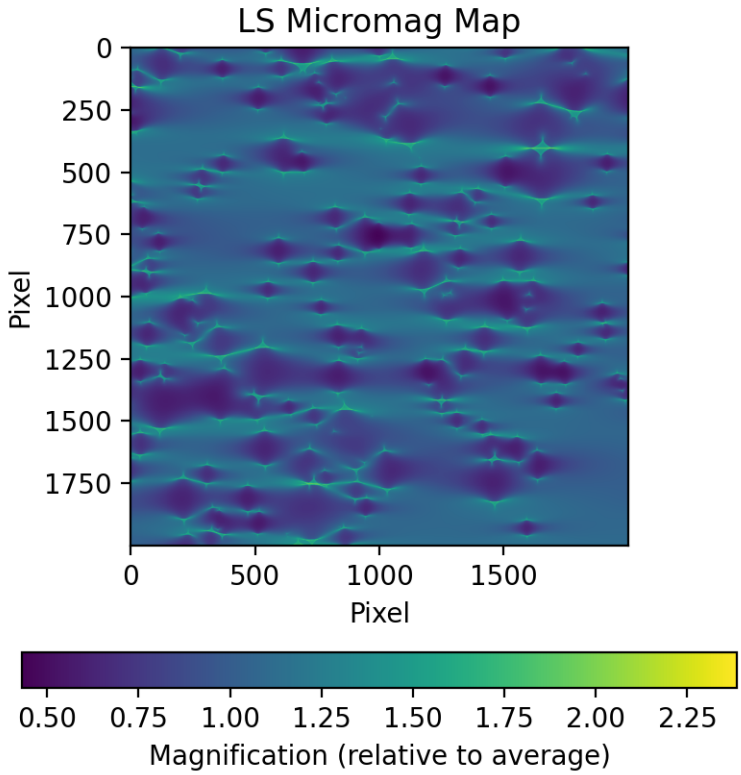

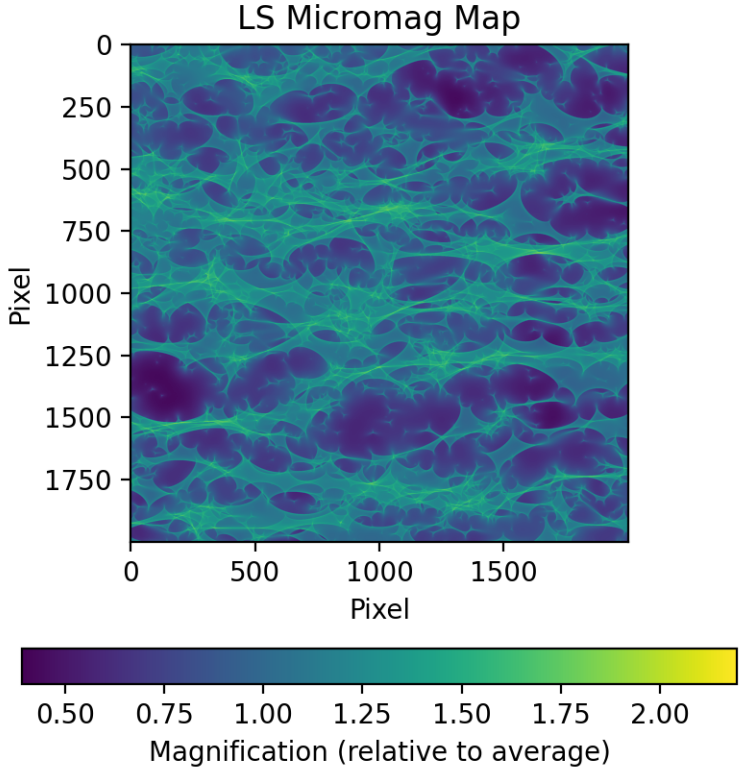

Figure 3-4: *Top:* Magnification map for lower saddle image for $S_j = 10\%$ *Bottom:* Magnification map for lower saddle image for $S_j = 100\%$

3.2 Dark Matter Distributions

The goal is to determine the probability of each stellar fraction for the lensing galaxy. To begin, I first find the probability distribution of microlensing effects, which is a histogram of the magnification maps for a given stellar fraction. I express these probability distributions as $P(\mu_{ij}|S_j)$, where $\mu_{ij} = \log_{10}(micromag_{ij})$, $i \in HM, HS, LM, LS$, and S_j is the stellar fraction for a given map j. The histograms in Figure 3-5 plot the logarithm of the magnification values in astronomical magnitudes for $S_j = 10\%$ and 100%.

3.2.1 Bayesian Analysis

The measurements of the X-ray fluxes of of each image come from multiplying the flux of all 4 images combined (via spectral fitting) by the individual fractions of the total flux (via two-dimensional image fitting). Dividing the flux of each image by their respective macrolensing magnitudes (Table A.1) gives four estimates of the instrinsic flux $F_{X,intr}$ of the quasar. The measured flux of each image is given by

$$\frac{f_{X,i}}{F_{norm}} = \frac{F_{X,intr}}{F_{norm}} * M_i * 10^{\mu_{ij}} \tag{3.1}$$

where M_i is the macro-magnification of image i. I choose $F_{norm} = 10^{-14}\frac{erg}{cm^2 s}$, which has no effect on the analysis. By taking the logarithm of this equation, we can solve for the instrinsic flux:

$$log_{10}\Big(\frac{F_{X,intr}}{F_{norm}}\Big) = log_{10}\Big(\frac{f_{X,i}}{F_{norm}}\Big) - log_{10}M_i - \mu_{ij} \tag{3.2}$$

where μ_{ij} is the x-axis in Figures 3-5.

The conditional probability of the lensing galaxy having a specific stellar fraction S_j is expressed as

$$P(S_j) = \sum_X P(S_j|X_{HM}, X_{HS}, X_{LS}, X_{LM})P(X) \tag{3.3}$$

where $X = log_{10}(F_{X,intr}/F_{norm})$, and X_i is the estimate of X from image i. By Bayes' theorem,

$$P(S_j|X_{HM}, X_{HS}, X_{LS}, X_{LM}) = \frac{P(X_{HM}, X_{HS}, X_{LS}, X_{LM}|S_j)P_{pr}(S_j)}{\sum P(X_{HM}, X_{HS}, X_{LS}, X_{LM}|S_j)P_{pr}(S_j)} \tag{3.4}$$

where $P_{pr}(S_j)$ is the a priori probability of S_j, which I take to be uniform, and the denominator is a normalization term. Combining $P_{pr}(S_j)$ with the denominator as the constant A results in

$$P(S_j|X_{HM}, X_{HS}, X_{LS}, X_{LM}) = A * P(X_{HM}, X_{HS}, X_{LS}, X_{LM}|S_j) \tag{3.5}$$

The contributions of each image to X are all physically distinct, so their probabilities are independent from each other. Thus, we can express

$$P(X_{HM}, X_{HS}, X_{LS}, X_{LM}|S_j) = \prod_i P(X_i|S_j) \tag{3.6}$$

Substituting equations 3.5 and 3.6 into equation 3.3 results in

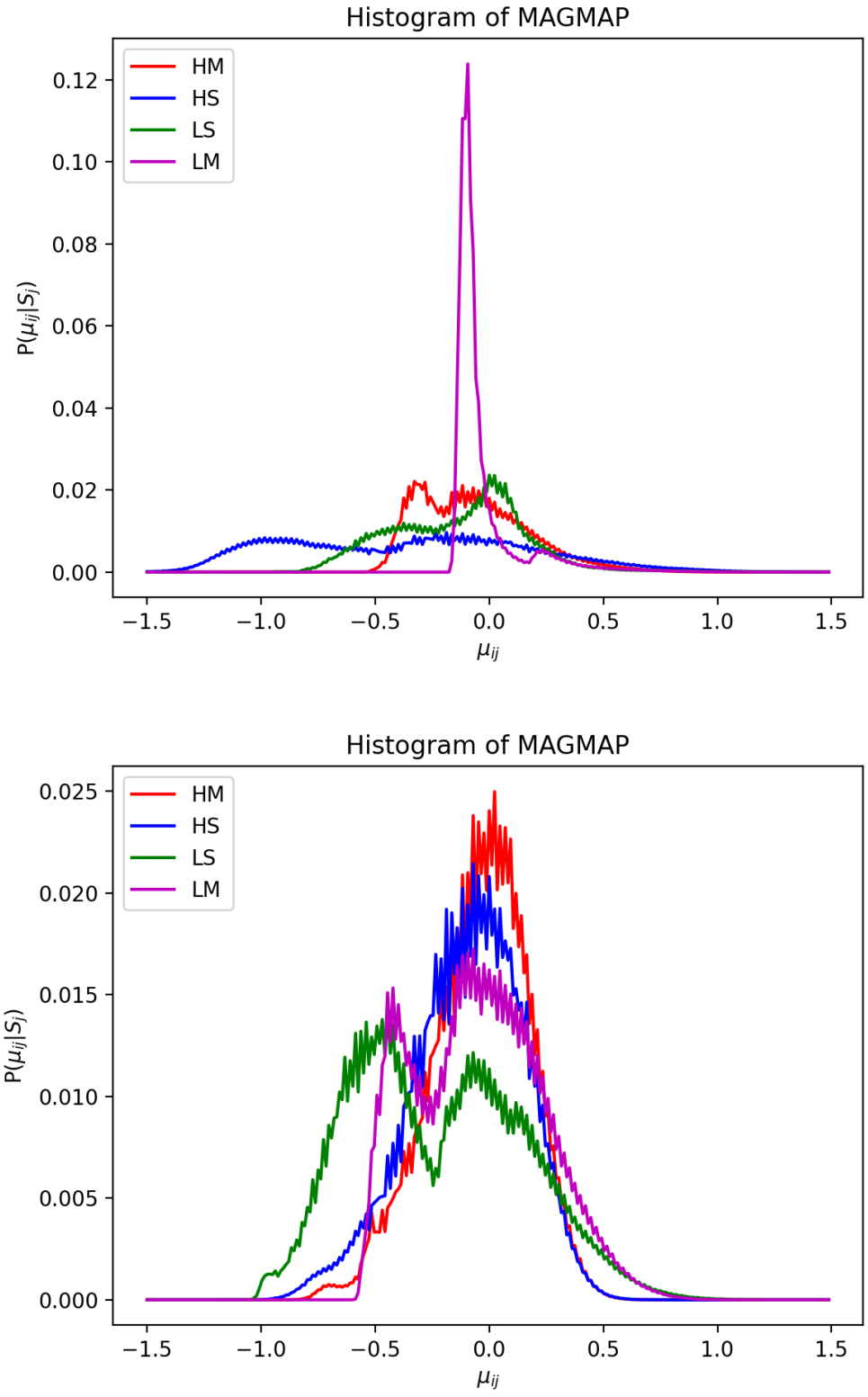

Figure 3-5: Normalized histograms of the logarithm of the pixel values in each microlensing magnification map. *Top:* $S_j = 10\%$ *Bottom:* $S_j = 100\%$.

$$P(S_j) = A * \sum_X \prod_i P(X_i|S_j)P(X) \tag{3.7}$$

I obtain $P(X_i|S_j)$ from the microlensing magnification histograms, the measured flux of each image $f_{X,i}$, and the macro-magnifications of each image in table A.1. The independent probability distributions for the intrinsic flux are plotted in Figure 3-6. Multiplying these together and introducing $G_j = \prod_i P(X_i|S_j)$ results in one probability distribution for the intrinsic flux given all four images in one observation. These are plotted in Figure 3-7. The integral of this probability distribution gives a measure of the relative likelihood for the assumed stellar fraction. I repeat the analysis for all stellar fractions to obtain the likelihood distribution of each stellar fraction. Once normalized, this is the probability distribution for the stellar fraction.

All of the above is for one observation, but each observation results in a different probability distribution for the intrinsic flux of the quasar given a certain stellar fraction. I integrate these intrinsic flux probability distributions and normalize them, resulting in a probability distribution for each stellar fraction for a single observation. I combine all observations using the conditional probability

$$P(S_j) = \prod_k P(S_j|obs_k) \tag{3.8}$$

where k represents one observation. This gives us the probability of the galaxy having a certain stellar fraction S_j. The results are plotted in Figure 3-8. It is clear from this plot that the most likely percentage of stars is 4.64% at a distance $\sim$ 6 kpc from the galaxy center. This means that the lensing galaxy is most likely 95.36% dark matter at this impact parameter.

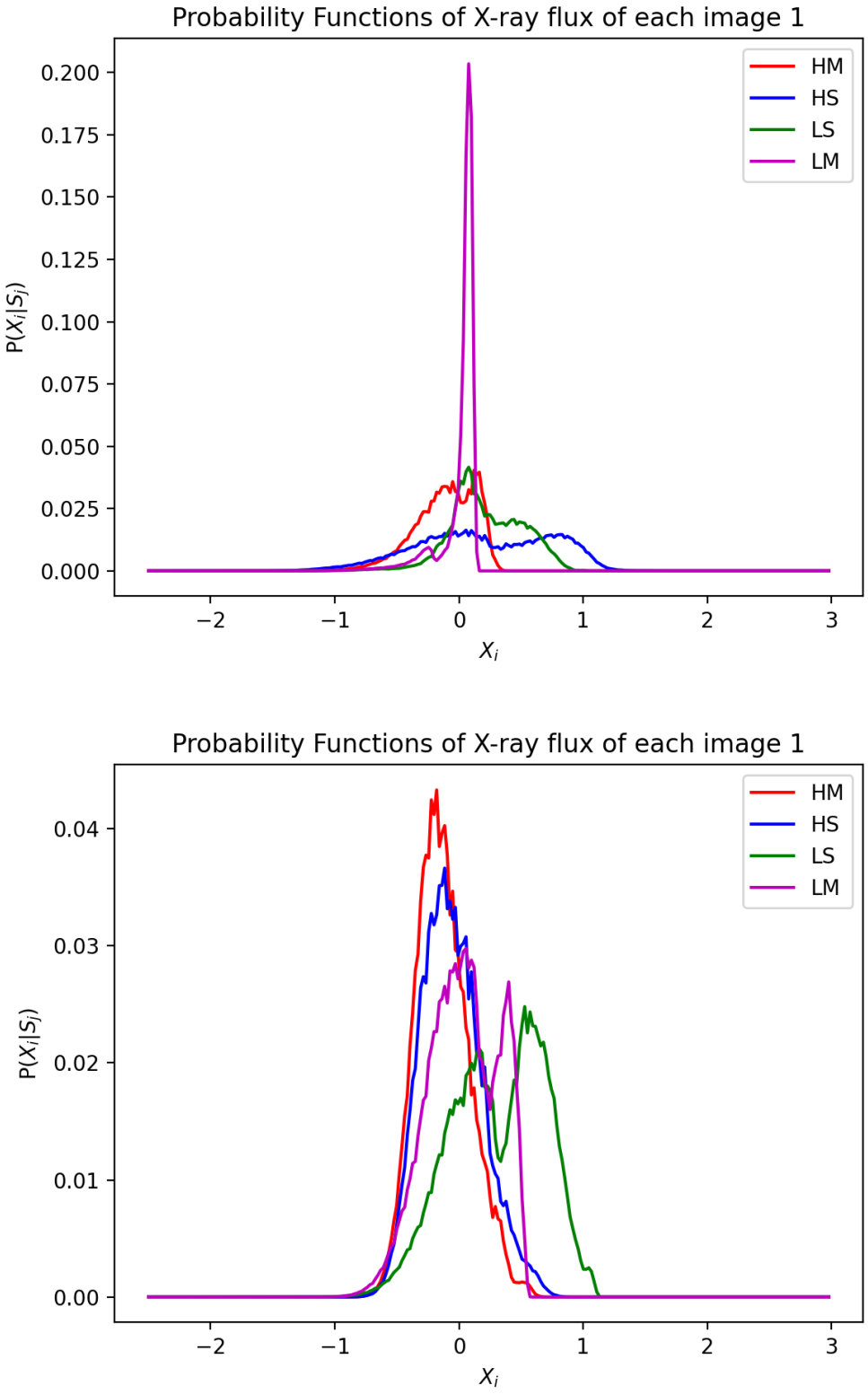

Figure 3-6: Independent probability distributions for the intrinsic flux of the quasar $F_{X,intr}$. *Top:* $S_j = 10\%$ *Bottom:* $S_j = 100\%$.

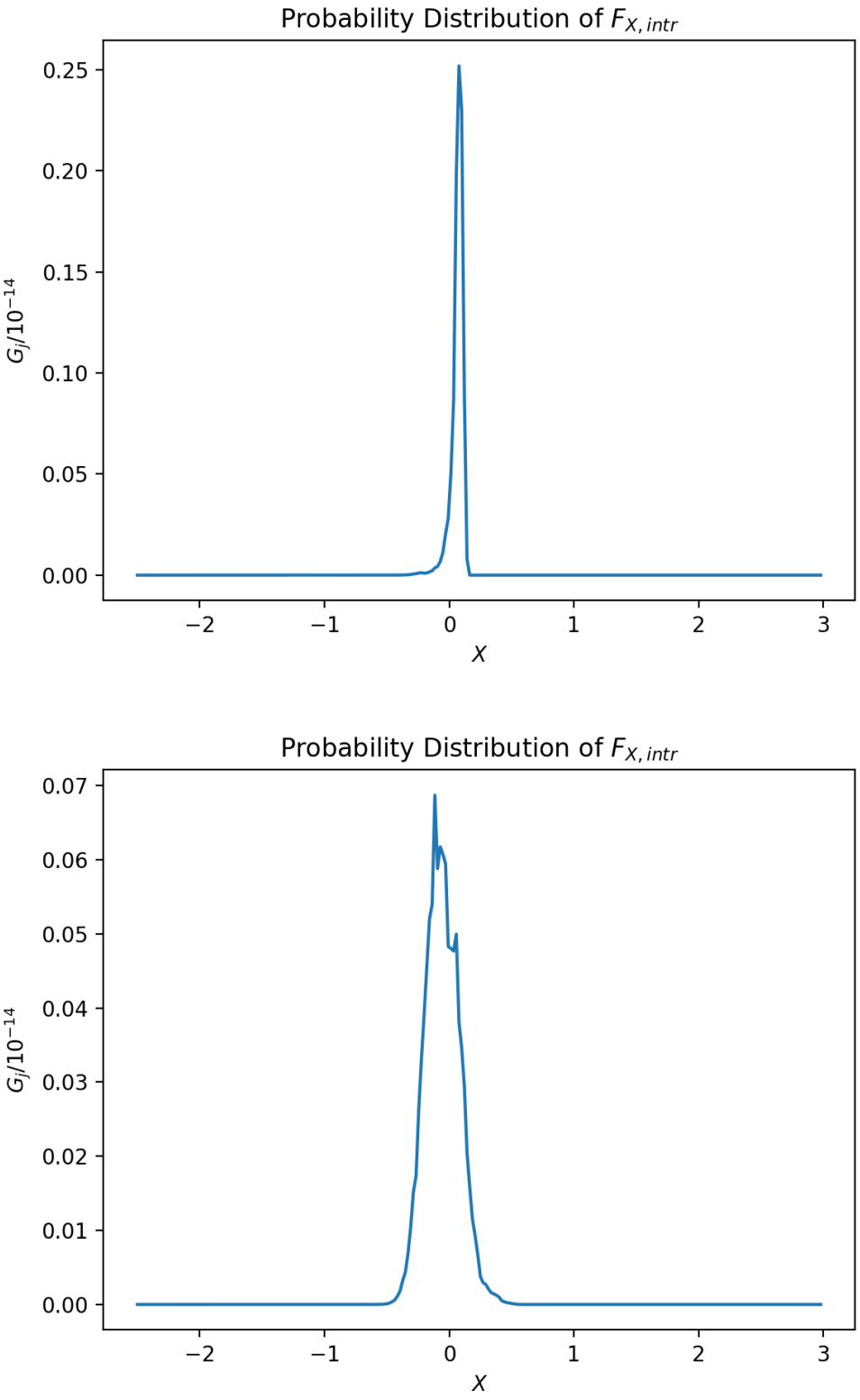

Figure 3-7: Total probability distribution for the intrinsic flux of the quasar $F_{X,intr}$. *Top:* $S_j = 10\%$ *Bottom:* $S_j = 100\%$.

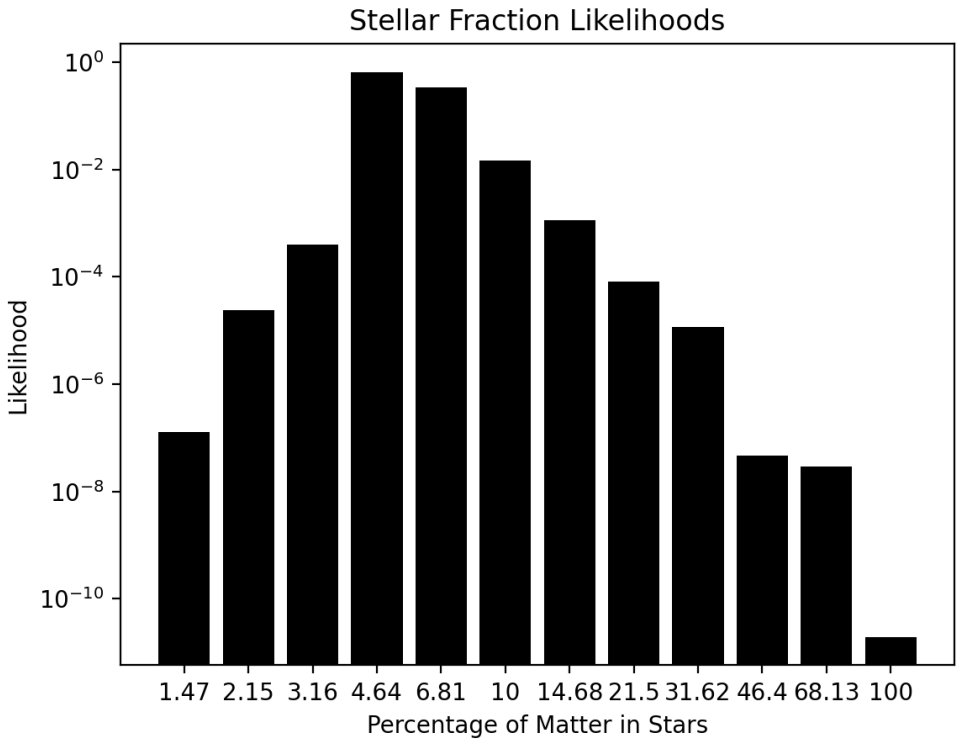

Figure 3-8: Probability of the distribution of matter integrated along the lines of sight to the quasar images.

Chapter 4

Conclusion

I have analyzed 9 publicly available *Chandra* observations of the quadruply lensed quasar PG1115. In testing different methods to reduce and fit the *Chandra* data, the best method involves the inclusion of the point spread function of the detector for each observation for the flux determinations of each image. The spectrum is best fit with a one dimensional power law, taking into account the absorption of the milky way.

I did not carry out the bayesian analysis with full consideration of the flux errors of each image. Further work with the inclusion of these errors will lead to higher confidence in the results, although this result is in agreement with past studies. Once more systems are analyzed, they can be combined to find the most likely stellar fraction for an ensemble of lensing galaxies.

I estimate the galaxy lensing quasar PG1115 to have 95.36% dark matter and 4.64% stellar matter at an impact parameter of $\sim$ 6 kpc. This is the same result as the previous analysis of this system (Pooley et al. 2012), but completed with updated Chandra Ray Tracer (Carter et al. 2003) and microlensing maps thanks to Jordan Koeller. This updated analysis needs to be applied to several other systems that have *Chandra* observations.

Appendix A

Tables

Image	Type	κ	γ	Magnification
A_1	HM	0.537	0.405	19.7
A_2	HS	0.556	0.5	-18.9
B	LS	0.658	0.643	-3.37
C	LM	0.472	0.287	5.09

Table A.1: Parameters of the Lensing Galaxy of PG1115

obsid	Date	Source Radius (arcsec)	Background Radius (arcsec)
363	2 June 2000	2.711	32.845
1630	3 November 2000	2.696	35.933
7757	31 January 2008	2.725	18.647
10730	2 November 2008	2.283	19.93
10795	9 February 2009	2.471	18.38
10796	27 March 2009	2.329	21.177
11857	1 February 2010	1.957	19.622
12093	7 February 2010	2.317	20.259
12094	15 February 2010	2.141	18.809

Table A.2: Source and background region sizes for observations of PG1115

obsid	Date	HM Fraction	HS Fraction	LM Fraction	LS Fraction	Total Flux/10^{-13} $\frac{erg}{cm^2 s}$
363	2 June 2000	$0.691^{+0.037}_{-0.041}$	$0.013^{+0.013}_{-0.013}$	$0.153^{+0.013}_{-0.012}$	$0.143^{+0.011}_{-0.011}$	$5.31^{+0.18}_{-0.18}$
1630	3 November 2000	$0.662^{+0.096}_{-0.060}$	$0.093^{+0.007}_{-0.024}$	$0.118^{+0.021}_{-0.017}$	$0.126^{+0.019}_{-0.014}$	$5.57^{+0.30}_{-0.26}$
7757	31 January 2008	$0.436^{+0.031}_{-0.024}$	$0.303^{+0.002}_{-0.022}$	$0.133^{+0.010}_{-0.010}$	$0.128^{+0.011}_{-0.010}$	$7.82^{+0.20}_{-0.20}$
10730	2 November 2008	$0.373^{+0.082}_{-0.053}$	$0.372^{+0.008}_{-0.050}$	$0.117^{+0.024}_{-0.026}$	$0.137^{+0.033}_{-0.024}$	$3.67^{+0.22}_{-0.20}$
10795	9 February 2009	$0.314^{+0.265}_{-0.044}$	$0.476^{+0.008}_{-0.051}$	$0.102^{+0.019}_{-0.028}$	$0.108^{+0.020}_{-0.017}$	$4.50^{+0.27}_{-0.24}$
10796	27 March 2009	$0.302^{+0.044}_{-0.037}$	$0.502^{+0.005}_{-0.056}$	$0.097^{+0.015}_{-0.014}$	$0.098^{+0.017}_{-0.016}$	$6.24^{+0.29}_{-0.33}$
11857	1 February 2010	$0.368^{+0.046}_{-0.038}$	$0.439^{+0.006}_{-0.055}$	$0.079^{+0.014}_{-0.013}$	$0.114^{+0.018}_{-0.017}$	$4.93^{+0.30}_{-0.26}$
12093	7 February 2010	$0.498^{+0.048}_{-0.042}$	$0.270^{+0.005}_{-0.034}$	$0.096^{+0.018}_{-0.015}$	$0.136^{+0.019}_{-0.016}$	$5.45^{+0.30}_{-0.31}$
12094	15 February 2010	$0.186^{+0.196}_{-0.039}$	$0.601^{+0.012}_{-0.164}$	$0.063^{+0.012}_{0.011}$	$0.149^{+0.018}_{-0.019}$	$4.86^{+0.26}_{-0.26}$

Table A.3: Chandra Observations and Flux Ratios of PG1115

Bibliography

Blackburne, J., et al., 10 July 2014, APJ, 789, 125

Carter, C. et al., 2003, ADASS XII ASP Conference Series, 295, 477

Cash, W., 1979, APJ, 565, 17

Chang, K. & Refsdal, S., 1979, Nature, 282, 561

Chartas, G., et al. 2020, Astro2020 Science White Paper

Kochanek, C. S., et al., 10 April 2004, APJ, 605, 58

Kochanek, C.S., 12 July 2004, The Ohio State University

Meneghetti, M., November 2016, National Institute of Astrophysics

Moustakas, L., et al. 2020, Astro2020 Science White Paper

Nelder, J. A., & Mead, R., 1965, Comput. J., 7, 308

Pooley, D., et al., 1 September 2006, APJ, 648, 67

Pooley, D., et al., 20 May 2007, APJ, 661, 19

Pooley, D., et al., 1 June 2009, APJ, 697, 1892

Pooley, D., et al., 10 January 2012, APJ, 744, 111

Pooley, D., et al. 2020, Astro2020 Science White Paper

Schechter, P., Wambsgnass, J., 5 September 2003, ASP, 1

Schechter, P., et al., 14 September 2014, IAU, 311

Tie, S. S., Kochanek, C. S., 13 September 2017, MNRAS, 473, 616

Wabsganss, J., 1990, PhD thesis Ludwig-Maximilians-Universitat Munich (preprint MPA 550)

Weymann, R. J., et al., 2 October 2980, Nature, 287, 416